Mark Fedorov, Jan Wrobel, Witold Chromińskia, Grzegorz Cieślak, Magdalena Płocińska, Krzysztof J. Kurzydłowski, Duc Nguyen-Manh

Composition stability of single phase in Cr-Fe–Mn-Ni alloys at high temperature: First-principles prediction and experimental validation

Composition stability of single phase in Cr-Fe–Mn-Ni alloys at high temperature: First-principles prediction and experimental validation

Mark Fedorov, Jan Wrobel, Witold Chromińskia, Grzegorz Cieślak, Magdalena Płocińska, Krzysztof J. Kurzydłowski, Duc Nguyen-Manh

Composition stability of single phase in Cr-Fe–Mn-Ni alloys at high temperature: First-principles prediction and experimental validation

Mark Fedorov[a], Jan S. Wróbel[a,*], Witold Chromiński[a,b], Grzegorz Cieślak[a], Magdalena Płocińska[a], Krzysztof J. Kurzydłowski[c] and Duc Nguyen-Manh[d]

[a]*Faculty of Materials Science and Engineering, Warsaw University of Technology, ul. Wołoska 141, 02-507, Warsaw, Poland*

[b]*NOMATEN Centre of Excellence, National Centre for Nuclear Research, ul. A. Sołtana 7, 05-400, Otwock, Poland*

[c]*Faculty of Mechanical Engineering, Białystok University of Technology, ul. Wiejska 45C, 15-351, Białystok, Poland*

[d]*CCFE, United Kingdom Atomic Energy Authority, Abingdon, OX14 3DB, United Kingdom*

ARTICLE INFO

ABSTRACT

The relative phase stability of face-centered cubic (fcc) and body-centered cubic (bcc) Cr-Fe-Mn-Ni alloys has been investigated using a combination of density functional theory (DFT), cluster expansion (CE) and Monte Carlo (MC) simulations. The MC simulations for bcc and fcc Cr-Fe-Mn-Ni alloys performed using the CE models described in this work and in our previous paper, respectively, have enabled to compute the difference between Gibbs free energies of 1767 fcc and bcc alloys in the whole composition range with a 5% composition step as a function of temperature. By applying a common tangent construction procedure and averaging over six pseudobinary sets, the regions of stability of fcc and bcc phases have been identified as well as the region of coexistence of both phases. For the latter, the fractions of fcc and bcc phases have been calculated using a lever rule. The results of MC simulations are in agreement with the available experimental data from the literature and the experiments performed within this work for the samples of $[CrFeMn]_{100-x}Ni_x$ ($x = 20, 25$ and 35) alloys synthesized using arc-melting and annealed at 1273 K for 48 hours. In particular, the fcc fractions obtained using the electron backscatter diffraction (EBSD) method for the as-cast and annealed samples are in line with the values from MC simulations. The analysis of fcc fractions of the near-equiatomic alloy compositions has enabled the identification of the best candidates that are predicted to be single fcc phase for a wide range of temperatures with 95 % confidence.

1. Introduction

High entropy alloys (HEAs) are the new class of materials containing four or more components in equal or near-equal atomic percent. They have been discovered by Cantor et al. [1] and Yeh et al. [2] in the year 2004 and have been found to possess unique microstructure and properties. The experiments show for example that these materials possess high strength and excellent wear, corrosion and irradiation resistance [2, 3, 4, 5, 6]. For example, yield strength and hardness in HEAs can display values in excess of 2000 MPa [7, 8] and 800 HV [9], respectively, and thus they are significantly larger than in the traditional alloys.

Due to the fact that the irradiation has a less detrimental effect on properties of some HEAs in comparison with pure metals as well as the conventional alloys [10, 11, 12, 13], HEAs are considered as potential candidates for applications in structural components of future fusion power plants and fission reactors of the next generation (Generation IV). In Ref. [12] it was reported that the swelling resistance of fcc Fe-Cr-Co-Mn-Ni alloy, also called Cantor alloy, under irradiation is 40 times higher than in pure fcc Ni. TEM analysis showed that voids in 5-component fcc HEA are significantly smaller than in pure Ni and FeNi alloy.

Unfortunately, the application of Cantor alloy in the fission and fusion power plants is undesirable due to the presence of cobalt that activates under irradiation. This motivated the materials scientists for the design of Co-free fcc Cr-Fe-Mn-Ni alloys for nuclear applications. As it was shown in Ref. [10], the radiation-induced segregation is much suppressed in fcc Cr-Fe-Mn-Ni alloy as compared with the Fe-Cr-Ni and Fe-Cr-Mn austenitic alloys. However, choosing optimal compositions of Fe, Cr, Mn and Ni are not straightforward. Since Cr is a bcc stabilizer, Ni is a fcc stabilizer, the ground state of Mn is the complex alpha structure, and Fe can possess either the bcc or fcc structure depending on temperature, it is difficult to predict the region of stability of fcc alloys in Cr-Fe-Mn-Ni system. Moreover, as it was presented in our previous work [14], formation of intermetallic phases might take place in a wide range of compositions especially at lower temperatures.

The experimental studies of HEAs from the Cr-Fe-Mn-Ni system in Refs. [10, 15, 16, 17, 18, 19, 20, 21, 22, 23, 24, 25, 26, 27] showed the complexity of phase stability of those alloys, which depends both on the composition of alloy and temperature. First of all, the equiatomic alloy decomposes into the fcc and bcc phase [18, 19, 24, 26]. A similar decomposition was also observed in $Cr_xFeMnNi$ (x=0.8, 1.0, 1.2, 1.5) in Ref. [26] whereas in $Cr_{24}Fe_{40}Mn_{28}Ni_8$ alloy from Ref. [23] there was found a presence of sigma (σ) phase. In Refs. [10, 15, 17, 20, 21, 22, 23, 25, 26, 27], there were reported also a few compositions that were characterized as

*jan.wrobel@pw.edu.pl

✉ markfedorov93@gmail.com (M. Fedorov); jan.wrobel@pw.edu.pl (J.S. Wróbel)
ORCID(s):

fcc single-phase alloys, including $Cr_{18}Fe_{28}Mn_{26}Ni_{28}$ proposed by the scientists from Oak Ridge National Laboratory (ORNL) that exhibited excellent irradiation properties [10]. Fcc single phase for the ORNL alloy was confirmed in Refs. [20] and [25]. The presence of Cr-rich bcc precipitates in the alloy with the same composition as the ORNL, both in the sample annealed at 1173 K and in the ion irradiated sample, was reported in Ref. [16]. The decomposition under ion irradiation was also observed for the alloy with similar composition, namely $Cr_{18}Fe_{29}Mn_{23}Ni_{30}$, but the MnNi precipitates were formed in that case.

The phase stability of Cr-Fe-Mn-Ni was investigated theoretically using the CALPHAD method [15, 21, 27], MD simulations [28] and DFT-based MC simulations [14]. In Ref. [28], the interatomic potential developed with the embedded atomic method for Cr-Fe-Mn-Ni alloys was applied to investigate, among others, the enthalpies of mixing of the fcc alloys in the Cr-Fe-Mn-Ni system and its subsystems. The authors noted the minimum and maximum values for the cohesive energy difference between the fcc and bcc phases. However, the regions of stability of fcc and bcc alloys have not been studied. In Refs. [15, 21, 27], the CALPHAD method was applied to investigate the phase stability as a function of temperature for chosen compositions. In Ref. [21], additionally, the phase diagrams for all ternary subsystems and the iso-chromium section of the Cr-Fe-Mn-Ni at a constant content of 20 at.% Cr at 1373 K have been reported. Despite the fact that the CALPHAD method is very useful for the prediction of phase stability of alloys, it has a few disadvantages. First, due to a limited number of experimental and theoretical data for alloys within the Cr-Fe-Mn-Ni, the databases applied in the CALPHAD method for HEAs are still not as trustful as the ones for traditional alloys. Moreover, the CALPHAD approximation is more applicable to the high-temperature interpretation of the phase diagram. Finally, it cannot be used for the generation of representative structures of alloys for further investigation of their properties using DFT or MD methods.

In order to investigate chemical ordering and the formation of ordered intermetallic phases in fcc Cr-Fe-Mn-Ni alloys, we developed in our previous work [14] the model for the fcc system combining the density functional theory (DFT) and cluster expansion (CE) method with Monte Carlo (MC) simulations. The MC simulations performed using the CE model have shown, among others, that there is a strong tendency to form the ordered intermetallic $L1_0$ MnNi phase for a wide range of compositions of Cr-Fe-Mn-Ni alloys. We found that this phase is present even for the ORNL composition that was characterized in a few papers as a single fcc phase alloy. This observation was recently confirmed experimentally in the irradiated alloy with a composition similar to the ORNL sample [17]. The other important observation was that the stability of random solid solutions could be increased by a decrease of concentration of Ni in comparison with the equiatomic composition [14]. However, as was mentioned previously, Ni is the fcc stabilizer, which means that the decrease of its content may destabilize the

fcc phase and cause the formation of the bcc phase or other more complex phases. In order to understand the relative stability of fcc and bcc alloys, the regions of stability of each of them and the regions of coexistence of both phases, in this work we decided to develop the DFT+CE model for the bcc Cr-Fe-Mn-Ni system to be able to compare the results of MC simulations for bcc alloys with those presented in Ref. [14] for fcc alloys and analyze the regions of stability and coexistence of fcc and bcc structures.

This paper is structured as follows. A section on methodology (Sec. 2) presents a short overview of the constructed models (Sec. 2.1) and the scheme we used to calculate the phase composition using models for fcc and bcc lattices (Sec. 2.2), as well as computational details and experimental methods used in this work (Sec. 2.3,2.4). Phase stability at 0 K, as obtained from DFT calculations, is described in Sec. 3. Finite-temperature phase stability, as obtained from MC simulations, is presented in Sec. 4, where we first analyze the difference between free energies of formation for fcc and bcc lattices (Sec. 4.1), then we find a region of coexistence of fcc and bcc and quantify it (Sec. 4.2), and finally illustrate the effect of each element on the relative phase stability (Sec. 4.3). Validation of our model is presented in Sec. 5, in which our theoretical results are compared with data available from the literature (Sec. 5.1), and with our own experimental results (Sec. 5.2). Lastly, we present in Sec. 6 a number of near-equiatomic compositions that are potentially single fcc phases. Conclusions are given in Sec. 7.

2. Methodology

2.1. A short overview of the model

A detailed description of the methodology can be found in the previous works of the authors [14, 29, 30, 31] and in the references therein. This work builds upon the previous work [14] on fcc Cr-Fe-Mn-Ni, adding into consideration a model for bcc Cr-Fe-Mn-Ni and subsequently studying the relative stability of Cr-Fe-Mn-Ni alloys with those lattices.

First, we calculate the mixing enthalpies H_{mix} of a set of structures that comprises the whole composition range of the investigated system, where each structure is described by a set of configuration variables $\vec{\sigma}$:

$$H_{mix}^{DFT}(\vec{\sigma}) = E_{tot}^{lat}(\vec{\sigma}) - \sum_{p=1}^{K} c_p E_{tot}^{lat}(p), \qquad (1)$$

where K is the number of alloy components and c_p are the average concentrations of p'th alloy component. In this work, we calculated mixing enthalpies from the Density Functional Theory (DFT) calculations with full relaxation and including collinear magnetism.

Then, we map the calculated H_{mix}^{DFT} to the simple-lattice-based Cluster Expansion model, where H_{mix}^{CE} are calculated as follows:

$$H_{mix}^{CE}(\vec{\sigma}) = \sum_{\omega,n,s} J_{\omega,n}^{(s)} m_{\omega,n}^{(s)} \langle \Gamma_{\omega',n'}^{(s')}(\vec{\sigma}) \rangle_{\omega,n,s}, \qquad (2)$$

where the summation is performed over all the clusters, distinct under symmetry operations in the studied lattice, represented by the following parameters: ω and n are the cluster size (the number of lattice points in the cluster) and its label (related to maximal distance between two atoms in the cluster), respectively; (s) is the decoration of cluster by point function $\gamma_{j,K}(\sigma_i)$. $m_{\omega,n}^{(s)}$ denotes the site multiplicity of the decorated clusters (in per-lattice-site units); and $J_{\omega,n}^{(s)}$ represents the Effective Cluster Interaction (ECI) energy corresponding to the same (s) decorated cluster.

$\langle \Gamma_{\omega',n'}^{(s')}(\vec{\sigma}) \rangle_{\omega,n,s}$ are the cluster functions, averaged over all the clusters of size ω' and label n' decorated by the sequence of point functions (s') that are equivalent by the symmetry to the cluster ω, n and decorated by the same sequence of point functions (s). Later in the text, $\langle \Gamma_{\omega',n'}^{(s')}(\vec{\sigma}) \rangle_{\omega,n,s}$ is referred to as $\langle \Gamma_{\omega,n}^{(s)}(\vec{\sigma}) \rangle$ for ease of notation. In Monte Carlo formalism, cluster functions are also averaged over the all MC steps at chosen temperature, which controls the accuracy and the computational costs of the calculations.

The definition of point functions in this work is the same as in Ref. [32] and as following:

$$\gamma_{j,K}(\sigma_i) = \begin{cases} 1 & \text{if } j = 0, \\ -\cos\left(2\pi \lceil \frac{j}{2} \rceil \frac{\sigma_i}{K}\right) & \text{if } j > 0 \text{ and odd,} \\ -\sin\left(2\pi \lceil \frac{j}{2} \rceil \frac{\sigma_i}{K}\right) & \text{if } j > 0 \text{ and even,} \end{cases} \quad (3)$$

where $i = 0, 1, 2, ...(K-1)$, j is the index of point functions $j = 0, 1, 2, ...(K-1)$ and $\lceil \frac{j}{2} \rceil$ stands for the ceiling function - rounding up to the closest integer.

The cluster function is then defined as the product of orthonormal point functions of occupation variables [33] $\gamma_{j,K}(\sigma_i)$, on specific cluster described by ω and n:

$$\Gamma_{\omega,n}^{(s)}(\vec{\omega}) = \gamma_{j_1 K}(\sigma_1)\gamma_{j_2 K}(\sigma_2) \cdots \gamma_{j_\omega K}(\sigma_\omega) \quad (4)$$

Using Structure Inversion Method, the optimal values of ECI are found that minimize the Cross-Validation Score between H_{mix}^{DFT} and H_{mix}^{CE}:

$$CVS^2 = \frac{1}{N} \sum_{i=1}^{N} (E_{DFT}^i - E_{CE'}^{(i)})^2, \quad (5)$$

where $E_{CE'}^{(i)}$ is the energy of the i-th structure, predicted by fitting CE energies to DFT energies, excluding E_{DFT}^i of the i-th structure.

ECI are used to parameterize Monte Carlo simulations, enabling us to calculate Gibbs free energy at finite temperatures.

Since we are interested in comparing the phase stability of two different lattices, we cannot compare H_{mix}, which is calculated with respect to different ground states for each lattice. Instead, we need to compare the formation enthalpies,

H_{form}, which can be calculated similarly to Eq. (1), but with respect to the global ground states (GS) of each element:

$$H_{form}^{DFT}(\vec{\sigma}) = E_{tot}^{lat}(\vec{\sigma}) - \sum_{p=1}^{K} c_p E_{tot}^{GS}(p), \quad (6)$$

where K is the number of alloy components and c_p are the average concentrations of p'th alloy component.

In the present study within the Cluster Expansion framework, H_{form} for fcc and bcc alloys can be obtained from H_{mix} by including the correction coming from each element:

$$H_{form}^{CE}(\vec{\sigma}) = H_{mix}^{CE,lat} + \sum_{p=1}^{K} c_p \left(E_{tot}^{lat}(p) - E_{tot}^{GS}(p) \right) \quad (7)$$

where $H_{mix}^{CE,lat}$ is calculated for each lattice using Eq. (2); $E_{tot}^{lat}(p)$ and $E_{tot}^{GS}(p)$ are the reference energies of p'th element in chosen lattice and p'th element in a true GS, respectively, calculated using DFT; K is the number of alloy components and c_p are the average concentrations of p'th alloy component.

At finite temperatures, entropy plays an important role in the stability of alloys. In this paper, we focus mainly on configurational entropy as the strongest entropic contribution to the free energy [33]. We use Bethe-Guggenheim quasichemical approximation [34, 35] for calculating the configurational entropy:

$$S_{conf}(\vec{\sigma}, T) = S_{ideal}(\vec{\sigma}) - \sum_n \frac{z_n}{2} I_n(\vec{\sigma}, T). \quad (8)$$

The first term in Eq.(8) represents the Bragg-Williams approximation[36]:

$$S_{ideal}(\vec{\sigma}) = -\sum_i c_i \ln c_i, \quad (9)$$

where c_i is the concentration of the ith element in the alloy.

The second term represents the lowering of entropy coming from the information about pair bonds with the length of the corresponding coordination shell, n, which can be expressed in terms of pair probability functions $y_{2,n}$:

$$I_n(\vec{\sigma}, T) = \sum_{ij} y_{2,n}^{ij}(\vec{\sigma}, T) \ln \frac{y_{2,n}^{ij}(\vec{\sigma}, T)}{c_i c_j}. \quad (10)$$

Pair probability functions are dependent on the atomic configuration and the temperature, $y_{2,n}^{ij}(\vec{\sigma}, T)$, but the notation will be shortened to $y_{2,n}^{ij}$ for better readability.

We can separate the terms coming from concentrations and pair probability functions in Eq. (10), and remembering that $\sum_j y_{2,n}^{ij} = c_i$, we can write:

$$I_n(\vec{\sigma}, T) = \sum_{ij} y_{2,n}^{ij} \ln \frac{y_{2,n}^{ij}}{c_i c_j} =$$

$$= \sum_{ij} y_{2,n}^{ij} \ln y_{2,n}^{ij} - \left(\sum_i \ln c_i \sum_j y_{2,n}^{ij} + \sum_j \ln c_j \sum_i y_{2,n}^{ij} \right) =$$

$$= \sum_{ij} y_{2,n}^{ij} \ln y_{2,n}^{ij} - \left(\sum_i \ln(c_i)c_i + \sum_j \ln(c_j)c_j \right) =$$

$$= \sum_{ij} y_{2,n}^{ij} \ln y_{2,n}^{ij} - 2 \sum_i c_i \ln c_i. \quad (11)$$

Substituting Eq.(9) and Eq.(11) into Eq.(8) we get:

$$S_{conf}(\vec{\sigma}, T) = S_{ideal}(\vec{\sigma}) - \sum_n \frac{z_n}{2} I_n(\vec{\sigma}, T) =$$

$$= -\sum_i c_i \ln c_i - \sum_n \frac{z_n}{2} \left(\sum_{ij} y_{2,n}^{ij} \ln y_{2,n}^{ij} - 2 \sum_i c_i \ln c_i \right) =$$

$$= \left(\sum_n z_n - 1 \right) \sum_i c_i \ln c_i - \sum_n \frac{z_n}{2} \sum_{ij} y_{2,n}^{ij} \ln y_{2,n}^{ij}. \quad (12)$$

The most correlation comes from the closest pairs, hence we consider the contribution only from the pairs with the distance of bond equal to 1st coordination shell. In fcc, the coordination number is equal to 12, hence:

$$S_{conf}^{fcc}(\vec{\sigma}, T) = 11 \sum_i c_i \ln c_i - 6 \sum_{ij} y_{2,1}^{ij} \ln y_{2,1}^{ij} \quad (13)$$

In bcc, the coordination number is equal to 8, hence:

$$S_{conf}^{bcc}(\vec{\sigma}, T) = 7 \sum_i c_i \ln c_i - 4 \sum_{ij} y_{2,1}^{ij} \ln y_{2,1}^{ij} \quad (14)$$

With formation enthalpies and configurational entropies considered, we can calculate the free energy of formation for each lattice:

$$G_{form}^{CE,lat}(\vec{\sigma}, T) = H_{form}^{CE,lat}(\vec{\sigma}, T) - T S_{conf}^{lat}(\vec{\sigma}, T), \quad (15)$$

which is used to estimate the relative phase stability at finite temperatures.

The magnetic and vibrational contributions to free energy are taken into account only in the form of correction to the fcc-bcc free energy difference from Ref. [37], dependent on the concentration of Fe, which stabilizes the fcc phase of Fe over the bcc phase in the temperature range between 1315 K and 1795 K and enables to reproduce the high-temperature γ-loop in Fe. Similarly as in Ref. [29], it is assumed that the correction is proportional to the concentration of Fe in the considered alloy.

2.2. Phase composition for multicomponent systems

A common tangent construction procedure with the subsequent lever rule calculations was applied to find the phase composition of MC simulated alloys (see Fig. 1).

For 3-component systems, we applied a pseudobinary approach, where the ternary phase diagram is "sliced" by the three sets of pseudobinaries, parallel to each X-Y binary (see Fig. 2). This produced satisfactory results for the fcc-bcc
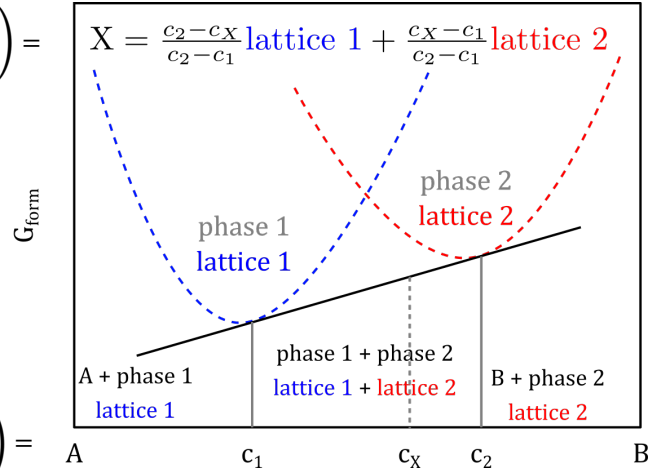

Figure 1: Schematic illustration of common tangent construction using free energies from two separate sets of simulations, represented by the blue and red curves.

separation lines, which served as a justification for applying this approach for the calculation of phase composition. However, since we calculate the phase composition along the line instead of a surface, the values of phase compositions should be averaged over all three sets, producing a smoothly varying composition space. The averaging is possible due to calculations being performed on a grid, which allows utilizing a similar procedure in a 4-component system, where there exist six binaries, and six sets of corresponding pseudobinaries, and therefore the averaging for each grid point is performed over six values. The error coming from such averaging is calculated as a standard error of the mean for each grid point. Using a dense grid increases the precision of the results obtained using this method.

2.3. Computational details

The ready model for fcc Cr-Fe-Mn-Ni has been taken from the authors' previous work [14], and the model for bcc has been created in a similar way as described therein, and in Refs. [29, 30, 38].

DFT calculations with collinear spin-polarization were performed using the projector augmented wave (PAW) method implemented in VASP [39, 40, 41, 42, 43, 44]. Exchange and correlation were treated in the generalized gradient approximation GGA-PBE [45]. The core configurations of Fe, Cr, Mn and Ni in PAW potentials were $[Ar]3d^7 4s^1$, $[Ar]3d^5 4s^1$, $[Ar]3d^6 4s^1$ and $[Ar]3d^9 4s^1$, respectively.

Total energies were calculated using the Monkhorst-Pack mesh [46] of k-points in the Brillouin zone, with the k-mesh spacing of 0.2 Å^{-1}. This corresponds to 12x12x12 k-point mesh for a four-atom fcc conventional unit cell or 14x14x14 k-point mesh for a bcc conventional unit cell. The plane wave cut-off energy used in the calculations was 400 eV. The total energy convergence criterion was set to 10^{-6} eV/cell, and force components were relaxed to 10^{-4} eV/Å.

Mapping DFT energies to CE was performed using the ATAT package [47, 48, 32, 49]. As described in Ref. [14],
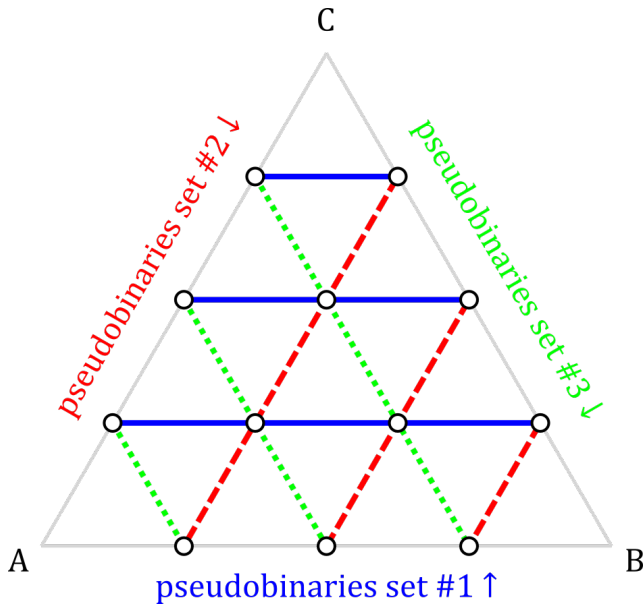
Figure 2: Schematic illustration of 3 sets of pseudobinaries in the ternary phase diagram. The phase composition is calculated for the compositions marked by open circles and averaged.

for fcc system, mapping of the mixing enthalpies of 835 structures was performed to achieve the cross-validation score of 13 meV. The set of clusters, which have minimized the CVS, consists of 6 two-body, 2 three-body and 1 four-body undecorated clusters.

For the bcc system, the final database consisted of 1062 structures, and the CVS is equal to 19 meV. The set of clusters, which have minimized the CVS, consists of 8 two-body, 1 three-body and 1 four-body undecorated clusters.

Size ω, label n, decoration (s), multiplicity $m_{\omega,n}^{(s)}$, coordinates of points and Effective Cluster Interactions $J_{\omega,n}^{(s)}$ (in meV) of aforementioned clusters for bcc system are listed in the Supplementary Material, Tables S1–S2 and Fig. S1. Effective cluster interactions for fcc Cr-Fe-Mn-Ni have been taken from our previous model and can be found in Table I in Ref.[14].

Semi-canonical MC simulations were also performed using the ATAT package separately for fcc and bcc lattices, containing 2048 atoms in the form of 8x8x8 fcc unit cells and 2000 atoms in the form of 10x10x10 bcc unit cells, respectively. For each composition, simulations were performed starting from a disordered high-temperature state at $T = 3000$ K. The alloy was then cooled down with the temperature step of $\Delta T = 100$ K, with 2000 equilibration and accumulation Monte Carlo passes. The aforementioned CVS can be converted into the errors of MC simulations, being equal to 150 K and 220 K for fcc and bcc models, respectively.

2.4. Experimental methods

The samples of three pseudo-binary alloys $[CrFeMn]_{100-x}Ni_x$ with three different Ni concentrations, $x = 20, 25$ and 35 at. %, and with other elements kept equiatomic, were synthesized using arc-melting and annealed at 1273 K for 48 h followed by water quenching. The microstructure and phase composition of as-cast and annealed samples were characterized using electron backscatter diffraction (EBSD) and scanning electron microscopy (SEM) combined with energy dispersive X-ray spectroscopy (EDS).

All the alloys were produced by the arc-melting method under an argon atmosphere. The high purity elements (Fe – Alfa Aesar 99.99% purity, Ni – Sigma Aldrich 99.95%, Mn – Sigma Aldrich 99.95%, and Cr – Alfa Aesar 99.99%,) were used. In all cases, the obtained ingots were re-melted at least three times to homogenize the composition. Obtained ingots have the form of round droplets with a weight of approximately 15 g.

Samples for SEM characterization were prepared with a conventional grinding with decreasing sand paper gradation and then polished mechanically to a mirror-like surface. Directly before observations, samples were gently cleaned with a low-energy argon plasma to enhance the signal-to-noise ratio. Observations were carried out with a Hitachi SU70 analytical scanning electron microscope equipped with a field emission gun. Observations conditions were set depending on the intention of the experiment and the recorded signal. EBSD maps were collected using Bruker e-flash HD detector, while data post-processing was done with Channel 5 software.

3. Zero-temperature properties

Formation enthalpies for fcc and bcc binary systems computed using DFT at 0 K are presented in Fig. 3. Among six binary systems, only in the case of the Fe-Cr system the bcc structures are more stable than the fcc structures for the whole range of compositions (see Fig. 3a). Moreover, there exist structures with slightly negative formation enthalpies in the Fe-rich region that were reported in the previous works [29, 50, 51]. There is also only one binary system, Mn-Ni, in which fcc phases are more stable for all concentrations (see Fig. 3f). It should be noted that L1$_0$ MnNi structure is the most stable intermetallic phase in the Cr-Fe-Mn-Ni system. For the remaining four binary systems, the convex hulls for the fcc and bcc structures intersect, meaning that there exists a region where the fcc phase should be more stable than the bcc phase and *vice versa*. In practice, in all of those systems, there exist regions of possible coexistence of the fcc and bcc phases, which are indicated in Figs. 3b–e by black dashed lines. The regions of coexistence of bcc and fcc at 0 K with negative formation enthalpies are observed for two systems, where ground states are fcc for one element and bcc for the other one, namely Cr-Ni (Fig. 3c) and Fe-Ni (Fig. 3e). Such regions are also present in ternary and quaternary alloys.

It should be noted that both fcc and bcc reference structures for Mn do not have $H_{form} = 0$, meaning that they are not ground states, see Figs. 3(b,d,f). The ground state for Mn is α-Mn, for which the unit cell consists of 58 atoms with four crystallographically inequivalent sites, each
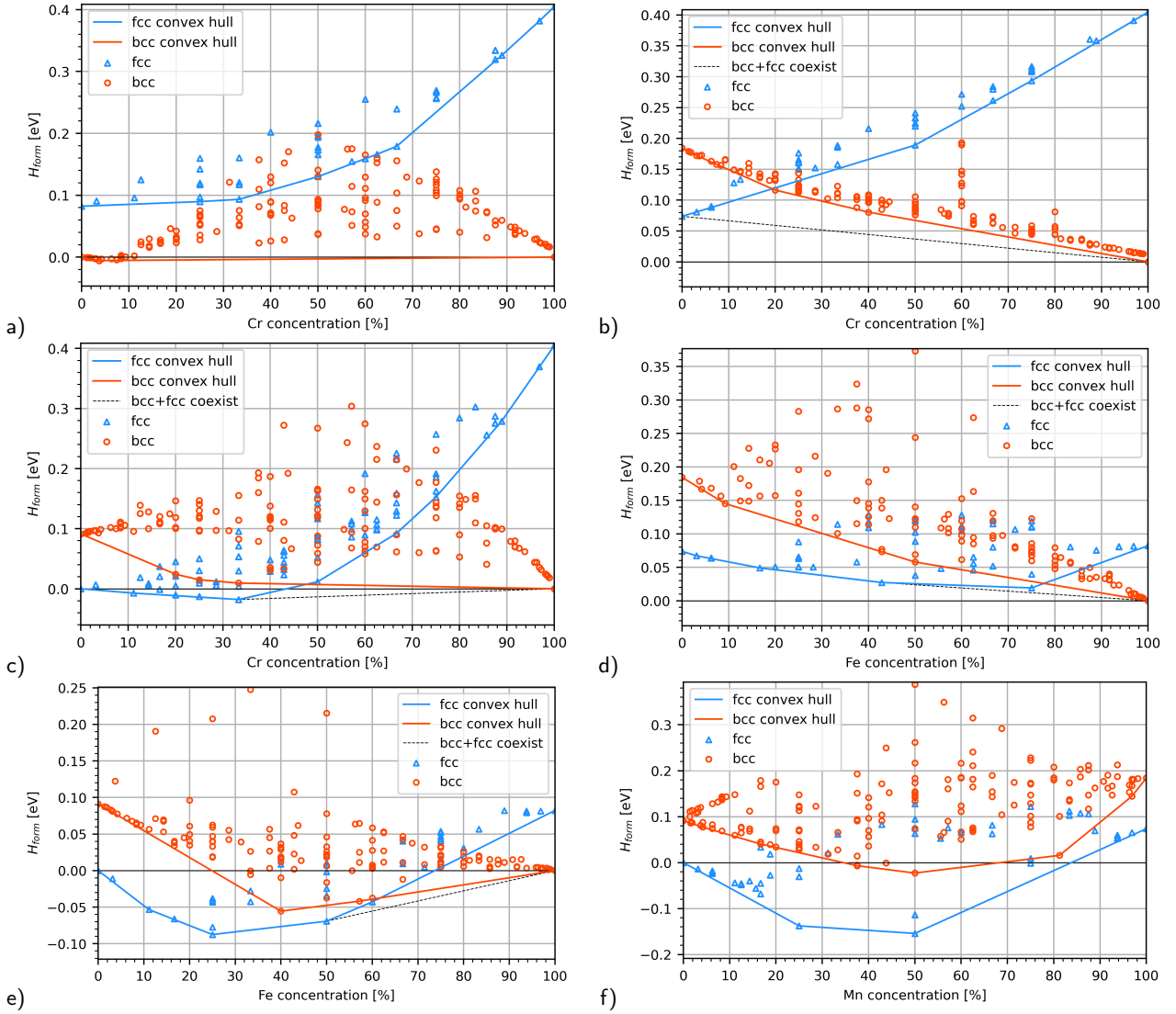
Figure 3: Enthalpies of formation computed using DFT for (a) Cr-Fe (b) Cr-Mn, (c) Cr-Ni, (d) Fe-Mn, (e) Fe-Ni and (f) Mn-Ni binary structures underlying fcc and bcc lattice. Blue and red lines are the convex hull for the fcc and bcc systems, respectively. The black dashed lines join the most stable fcc and bcc structures and indicate the regions of possible coexistence of fcc and bcc phases at 0 K.

divided into two magnetically inequivalent sites, ordered antiferromagnetically. Since this is a complex phase, its stability is limited to the Mn-rich region [52], which is out of the scope of the current work.

Unlike for the fcc system, no stable ternary or quaternary intermetallic phases were found in bcc Cr-Fe-Mn-Ni system from our DFT calculations. Stable intermetallic phases in fcc Cr-Fe-Mn-Ni alloys are shown in Table II of our previous work [14].

4. Finite-temperature phase stability

In order to investigate the fcc-bcc phase stability of Cr-Fe-Mn-Ni alloys at elevated temperatures, the effective cluster interactions for the bcc system, described in the previous section, and for the fcc system, described in our previous paper [14], were applied in MC simulations for a

compositional grid, where the concentration of each element is changed in a step of 5 at.%, consisting of total 1767 compositions (excluding four compositions which are pure elements).

4.1. Fcc-bcc free energy difference

Free energies of formation were calculated based on formation enthalpies from MC simulations and configurational entropies, obtained from pair correlation functions, as described in Section 2.1. Additionally, the magnetic and vibrational correction was applied to the fcc-bcc free energy difference from Ref. [37], also described in Section 2.1.

The calculations of configurational entropies using a pair-wise approximation from Eqs. 12–14 produce reasonable entropy values in the high-temperature region, approaching ideal values (Eq. 9), but often underestimate the entropy values in the low-temperature limit, where even
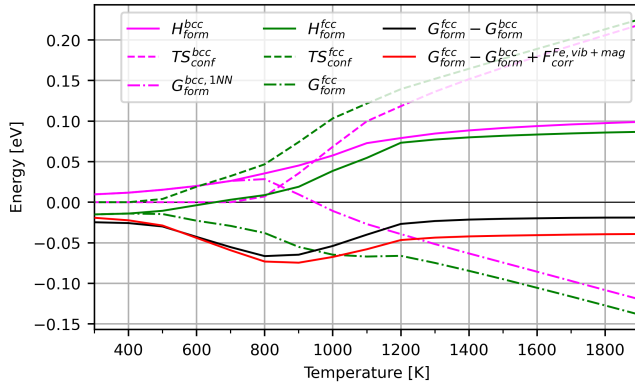
Figure 4: G_{form} and its contributions for equiatomic Cr-Fe-Mn-Ni in fcc and bcc lattices, as well as the difference between G_{form} without and with magnetic and vibrational correction for Fe, which helps to reproduce high-temperature γ-phase.

negative values may be obtained [53]. Such negative values of entropy arise from the presence of long-range ordered precipitates forming in the alloy, for which, in practice, the entropy would be equal or very close to zero. As such, only positive values of entropies for all structures were taken into account in the subsequent calculations of G_{form}. In effect, this reduces the overestimation of G_{form} of the fcc phase coming from entropy consideration since configurational entropy from a pair-wise approximation in fcc structures is usually higher than in bcc structures.

Since negative entropy is obtained both in bcc and fcc structures in the low-temperature limit, the relative stability in this region is calculated for the same thermodynamic potentials. However, there exist compositions between high- and low-temperature limits, for which the negative entropy is obtained only for one of the considered lattices. For such cases, the estimation of relative stability in mid-temperature regions has a lower precision with an error that is hard to estimate.

Contributions to G_{form} are shown in Fig. 4, as well as the difference between G_{form}^{fcc} and G_{form}^{bcc}. The effect of the correction $F_{corr}^{Fe,vib+mag}$, discussed at the end of Section 2.1 is also visible in this figure: it increases the stability of fcc lattice (for compositions with Fe) at higher temperatures, and decreases it's stability at lower temperatures.

In Figs. 5a and 5b, there are shown the differences between the free energies of formation for fcc and bcc alloys at temperatures 800 K and 1300 K for the whole concentrations range. The free energy differences have the most negative values for the Ni-rich alloys and the most positive values for the Cr-rich alloys. As it is shown in Figs. 5a and 5b, the points of intersection between the free energies of fcc and bcc alloys form different surfaces in the composition space depending on the temperature. With temperature increase, the surface of intersection points reduces in area and moves in the direction of Cr-rich compositions at temperature 1300 K compared to temperature 800 K, meaning that the stability of the fcc phase in the near-equiatomic region increases at

higher temperatures. Responsible for that are differences in enthalpies of formation and configurational entropy of fcc and bcc alloys as well as vibrational and magnetic correction. It is important to note that the intersections between the free energies of formation of fcc and bcc alloys do not divide the phase diagram into the regions of stability of single-phase fcc and bcc alloys. As it was shown in Ref. [26], the experimental results for $Cr_xFeMnNi$ alloys ($x = 0.8$, 1.0, 1.2 and 1.5) reveal that there is observed a coexistence of two phases for a wide range of compositions.

4.2. Coexistence of fcc and bcc phases

In order to study the coexistence of fcc and bcc phases and their fractions in Cr-Fe-Mn-Ni alloys, we applied the common tangent construction procedure, as it was described in Section 2.2. This method enabled the prediction of the atomic fraction of fcc and bcc phases for 1767 alloy compositions in the whole concentration range in the 5 at. % concentration mesh for the temperatures between 300 K and 1900 K. Further in the text, an atomic fraction in theoretical results is simply referred to as a fraction. In Figs. 5c and 5d, there are shown the fcc fractions at two temperatures, 800 K and 1300 K. For the sake of clarity of presentation, the results are shown only for 10 at.% concentration mesh. The whole database of results is provided in the Supplementary Material. As in the case of differences in the free energies of formation, there is a notable variation in the results at those two temperatures. In addition to the fcc Ni-rich and bcc Cr-rich regions in composition space, there are visible points with the coexistence of fcc and bcc phase, which are located around the region of intersections of fcc and bcc free energies, indicated in Figs. 5a and 5b using black points, and the region of coexistence is spanned into the Fe-rich region for the results at 1300 K.

4.3. The influence of element concentration on phase stability

In order to understand the influence of the concentration of each element on the fcc-bcc phase stability at the whole temperature range, we studied the temperature dependence of the fcc fraction in pseudo-binary $[ABC]_{100-x}D_x$ alloys, where the concentration of one element, x was varying from 0% to 95% with 5% concentration step and the concentrations of other elements were kept equiatomic. The fcc fraction of pseudo-binary alloys as a function of Cr, Fe, Mn and Ni concentration are shown in Figs. 6a–6d, respectively. As described in Section 2.2, the values presented in Fig. 6 are averaged over 6 pseudo-binary sets. The errors of such averaging are calculated as standard errors with 95% confidence interval. As shown in Figs. 7a–7d, the errors can be significantly different depending on the alloy composition and temperature. The highest errors throughout the whole composition range are observed in the regions with the coexistence of fcc and bcc phases.

Similar to the Schaeffler diagram for Fe-Cr-Ni steels [54], in the case of Cr-Fe-Mn-Ni alloys, there is observed an effect of stabilization of fcc and bcc phase by Ni and Cr
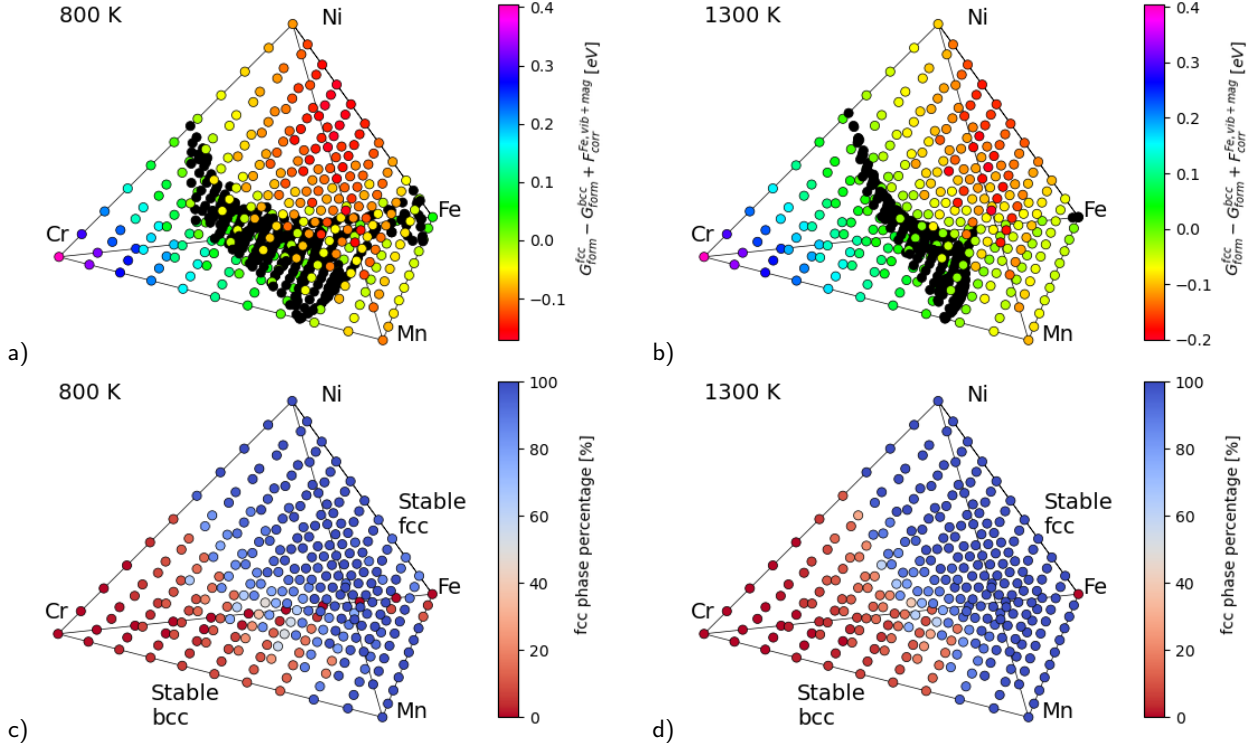
Figure 5: (a,b) The fcc-bcc free energy difference and (c,d) the fraction of fcc phase in the Cr-Fe-Mn-Ni alloys obtained using MC simulations at (a,c) 800 K and (b,d) 1300 K. Black points indicate the intersections of fcc-bcc free energies of formation.

that are shown in Figs. 6a and 6d, respectively. According to DFT-based MC simulations, the single fcc phase is fully stable at all temperatures for alloys with Cr content equal to or smaller than 10 at. % Cr, see Fig. 6a. For Cr concentrations equal to 15 and 20 at. %, the bcc fraction is not larger than 4 %, which is below the error bars corresponding to the results for those compositions. It means that with 95 % confidence, the single fcc phase is also stable for those alloy compositions. If not, it may possibly exist only in a narrow range of temperatures, see Fig. 6a. With 95% confidence, the single bcc phase can be observed for all Cr concentrations larger than 50 at. % Cr. However, the errors increase with a decrease of temperature and Cr concentration, see Fig. 7a, which means that some small fraction of the fcc phase might be possibly observed for alloys with lower Cr content and lower temperature. For the pseudo-binary alloys with Cr concentration between 30 and 50 at. % Cr, the fcc and bcc phases should coexist. A special and important case is the equiatomic composition with 25 at. % of each element, for which the fraction of fcc phase is significantly decreased, down to 91 %. The error for that temperature is equal to 9 %, which means that with 95% confidence, the fcc phase can still be observed, however, the coexistence of the two phases is possible.

In contrary to Cr, Ni is a fcc phase stabilizer and the fcc phase is with 95 % confidence stable for the pseudo-binary alloys with Ni content higher than 25 at. %, see Fig. 6d. If the bcc fraction is observed, its percentage is not larger than 6 % and usually smaller than 2 %, which is below the errors

provided for considered compositions and temperatures in Fig. 7d. In contrary to Cr-rich alloys, the Cr-Fe-Mn-Ni alloys with a low Cr concentration consist of the bcc phase in the majority.

As shown in Fig. 6b, similarly to pure Fe, the fcc fraction of Fe-rich alloys is strongly dependent on temperature. The bcc fraction is dominant at low temperatures, for example, below 1000 K for the pseudo-binary alloy with 95 at. % Fe, whereas at higher temperatures, the fcc phase becomes stable. The fcc-bcc phase transition temperature decreases with a decrease of Fe content, and for the alloy with 55 at. % Fe, the single fcc phase is formed above 500 K.

The influence of Mn on the relative fcc-bcc phase stability of $[CrFeNi]_{100-x}Mn_x$ pseudo-binary alloys is shown in Fig. 6c. The investigation of that effect is potentially important for the design of Cr-Fe-Mn-Ni-based high-entropy alloys since those materials contain a significantly higher concentration of Mn than austenitic steels. Interestingly enough, the fcc phase is dominant for the pseudo-binary alloy with all considered Mn concentrations and temperatures. As it was discussed in our previous paper [14], the stability of the fcc phase in alloys containing Mn and Ni atoms is strongly related to the formation of the intermetallic $L1_0$ MnNi phase. The fcc fraction in the $[CrFeNi]_{100-x}Mn_x$ pseudo-binary alloys is usually higher than 90 % and, for the majority of compositions, the bcc fraction is smaller than the errors provided in Fig. 7c for corresponding compositions and temperatures. Therefore, with 95 % confidence, the single fcc phase can be observed for most of $[CrFeNi]_{100-x}Mn_x$ alloys.
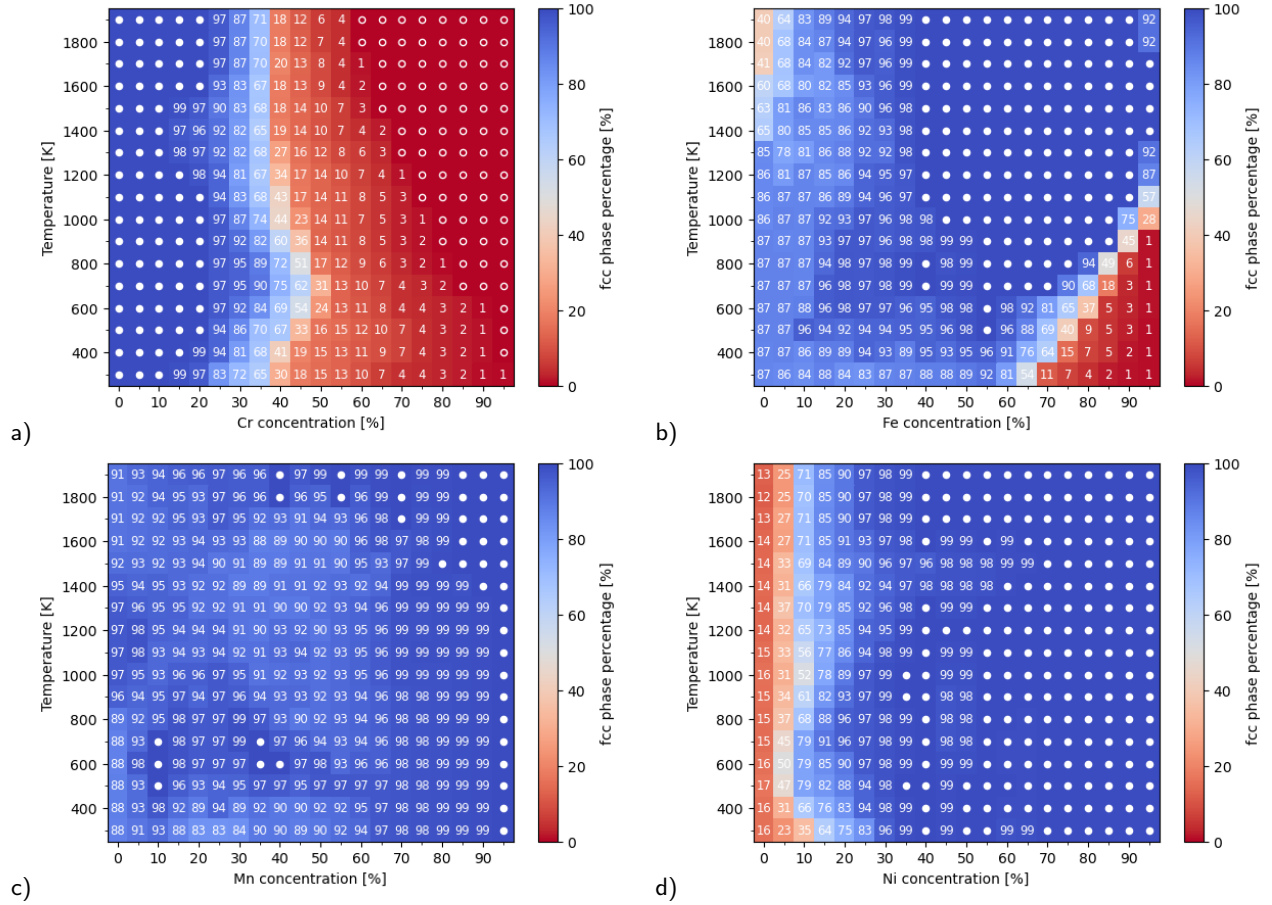
Figure 6: Heatmap showing fcc fraction in the Cr-Fe-Mn-Ni alloys according to the common tangent as a function of temperature and concentration of (a) Cr, (b) Fe, (c) Mn and (d) Ni. In order to improve the readability of the figure, 100% fcc is marked with filled circles (•), and 0% fcc is marked with open circles (o).

However, it should be noted that since α-Mn GS phase is not considered in this work, the phase of the structures in the Mn-rich region is not likely to be fcc, but rather α-Mn solid solution.

5. Experimental validation of the model

In order to validate the model, we compared the results of fcc-bcc phase stability of Cr-Fe-Mn-Ni alloys computed using DFT-based MC simulations with the experimental results available in the literature as well as those performed within this work.

5.1. Comparison with the experimental data from previous works

In Table 1, there are presented phase compositions of alloys investigated experimentally in Refs. [15, 17, 21, 22, 23, 26, 27] and compared with the results from DFT-based MC simulations. Since heat treatment of most experimental samples consisted of homogenization and annealing at two different temperatures, the results of MC simulations are also given for two corresponding temperatures. As shown in Table 1, the fraction of the fcc phase from MC simulations generally agrees with the experimental observations.

In particular, the theoretical model predicts no fraction of bcc phase for the alloy compositions characterized experimentally as single fcc phase and reported in Refs. [15, 17, 21, 22, 23, 27], see Table 1. The results of simulations also show correctly the stability of the single fcc phase for $Cr_xFeMnNi$ alloy with $x = 0.8$ and the coexistence of fcc and bcc phases for $x = 1.0, 1.2$ and 1.5, reported in Ref. [26]. The theoretical model correctly predicts the decrease of stability of the fcc phase with the increase of Cr content in the alloy. However, the fraction of the bcc phase from MC simulations and the averaging procedure is overestimated compared with experiments. It can be caused by the approximations applied in the model as well as the relatively short annealing time that might not be enough to reach the thermodynamic equilibrium state simulated using the exchange MC simulations.

5.2. Comparison with the experiments performed within this work

In order to have more experimental results for the validation of our model, we synthesized using arc-melting and characterized the as-cast samples and the samples annealed at 1273 K for 48 h, as described in Section 2.4. Since
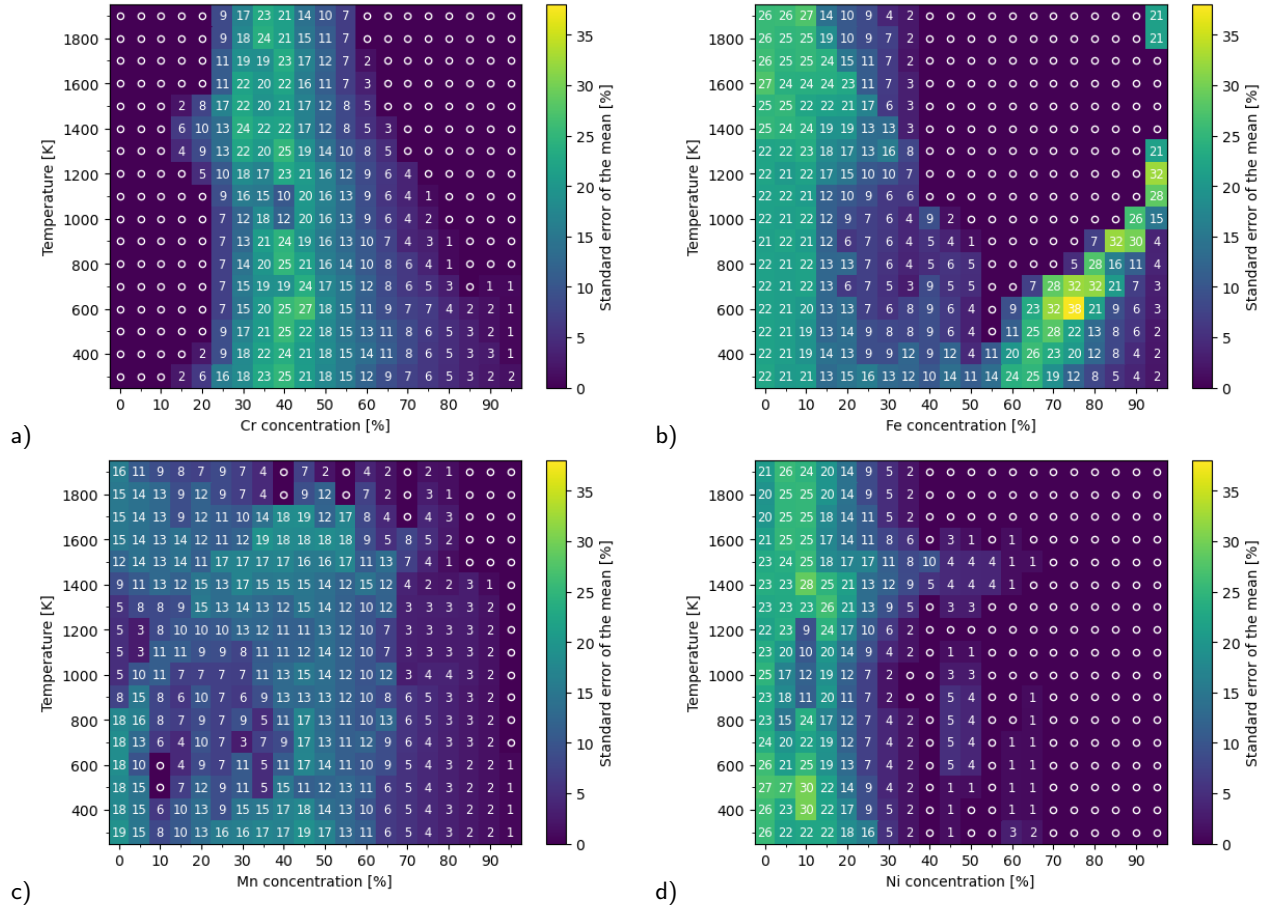
Figure 7: Heatmap showing standard errors of the mean fcc fraction for the Cr-Fe-Mn-Ni alloys as a function of temperature and concentration of (a) Cr, (b) Fe, (c) Mn and (d) Ni, coming from the averaging of the results over six pseudo-binary sets.

Ni is the main fcc stabilizer and, as it was shown in our previous paper [14], it has the most prominent impact on the order-disorder transition temperature, we focused on pseudo-binary alloys with three different Ni concentrations, namely 20, 25 and 35 at. % Ni, with other elements kept equiatomic.

In Fig. 8, there are shown the results of EBSD characterization of as-cast and annealed samples. In the case of as-cast samples, the coexistence of fcc and bcc phase is observed only for the $[CrFeMn]_{80}Ni_{20}$ alloy, see Fig. 8a, whereas the samples with 25 and 35 at. % Ni are single fcc phase, see Figs. 8b and 8c. In particular, as reported in Refs. [24, 18, 19, 26], there is no decomposition of the as-cast equiatomic fcc Cr-Fe-Mn-Ni alloy into bcc or σ phases. However, such a decomposition is clearly visible in the EBSD pattern for the annealed sample of equiatomic alloy. It is worth noting that there is a coexistence of three phases, namely fcc, bcc and σ phase. The presence of the σ phase within the fcc medium and high entropy alloys containing the binaries Cr-Fe, Cr-Mn or the ternary Cr-Fe-Mn [55, 56] subsystems has been widely reported in the recent investigations [3, 57, 58, 59]. For example, in the Cantor alloy, the σ phase is found to be significantly enriched in Cr, and also contained some Mn, Fe and Co, but very little Ni. The crystal structure was found

to be tetragonal, with lattice parameters of $a \approx 8.8$ Å and $c \approx 4.5$ Å [57], consistent with the well-known σ phase in Cr-Fe binary ($a = 8.799$ Å and $c = 4.546$ Å) [60]. The latter one is related to the A2 (bcc solid solution) kinetic phase transformation from the high-temperature [61]. In the case of alloy with 20 at. % Ni, the bcc phase observed in the as-cast sample is transformed to the σ phase in the annealed sample, compare Figs. 8a and 8d. The $[CrFeMn]_{65}Ni_{35}$ alloy is a single fcc phase both for the as-cast sample as well as the annealed sample.

The area fractions of fcc, bcc and σ phase in the as-cast and annealed samples of Cr-Fe-Mn-Ni alloy are summarized and compared with theoretical results in Table 2. Since the temperature related to the as-cast state is unknown, the experimental data are compared with the MC results for temperatures between 1100 K and 1500 K.

In agreement with the results from EBSD characterization, the lowest fraction of the fcc phase obtained from MC simulations is observed for the alloy with 20 at. % Ni. However, theoretical values seem to be slightly overestimated both for the as-cast and annealed sample, which can be explained by the errors related to the averaging procedure, described in Section 2.2 and 4.3. The MC simulations for the equiatomic alloy show a much smaller fcc fraction than

Composition		Treatment	Phase composition				
			Exp.	Monte Carlo simulations			
					T [K]		T [K]
$Cr_{12}Fe_{64}Mn_{12}Ni_{12}$		homogenized at 1473 K 10h,	fcc	fcc	1500	fcc	1300
$Cr_{12}Fe_{60}Mn_{16}Ni_{12}$	[15]	air-cooled, cold-rolled (50%), annealed	fcc	fcc	1500	fcc	1300
$Cr_{12}Fe_{56}Mn_{20}Ni_{12}$		at 1273 K for 1h, furnace-cooled	fcc	fcc	1500	fcc	1300
$Cr_{18}Fe_{29}Mn_{23}Ni_{30}$	[17]	homogenized at 1473 K 18h, quenched	fcc	99±2% fcc	1500		
$Cr_{20}Fe_{35}Mn_0Ni_{45}$			fcc	fcc	1400	fcc	1200
$Cr_{20}Fe_{30}Mn_5Ni_{45}$		annealed at 1373 K 24h, cold-rolled	fcc	fcc	1400	fcc	1200
$Cr_{20}Fe_{35}Mn_5Ni_{40}$	[21]	(80%), annealed at 1173 K 1h,	fcc	fcc	1400	fcc	1200
$Cr_{20}Fe_{30}Mn_{10}Ni_{40}$		gas-quenched	fcc	fcc	1400	fcc	1200
$Cr_{13}Fe_{50}Mn_{27}Ni_{10}$	[22]	cold-rolled, annealed at 1173 K 1h	fcc	fcc	1200		
$Cr_4Fe_{40}Mn_{28}Ni_{28}$			fcc	fcc	1300	fcc	1100
$Cr_{12}Fe_{40}Mn_{28}Ni_{20}$		homogenized at 1273 K 24h, cold-rolled	fcc	fcc	1300	fcc	1100
$Cr_{18}Fe_{40}Mn_{28}Ni_{14}$	[23]	(80%), annealed at 1123 K 30m	fcc	99±3% fcc	1300	100±1% fcc	1100
$Cr_{24}Fe_{40}Mn_{28}Ni_8$			fcc+σ	91±15% fcc	1300	88±17% fcc	1100
$Cr_{21}Fe_{26}Mn_{26}Ni_{26}$			fcc	95±10% fcc	1500	99±2% fcc	1100
$Cr_{25}Fe_{25}Mn_{25}Ni_{25}$	[26]	homogenized at 1473 K 6h, forged,	99% fcc	90±17% fcc	1500	94±9% fcc	1100
$Cr_{29}Fe_{24}Mn_{24}Ni_{24}$		annealed at 1073 K 1h	91% fcc	85±21% fcc	1500	85±14% fcc	1100
$Cr_{33}Fe_{22}Mn_{22}Ni_{22}$			77% fcc	69±21% fcc	1500	70±15% fcc	1100
$Cr_{20}Fe_{35}Mn_{10}Ni_{35}$	[27]	water-cooled, homogenized at 1273 K 12h, water-cooled	fcc	fcc	1300		
$Cr_{18}Fe_{27}Mn_{27}Ni_{28}$	[10]	homogenized at 1473 K for 48h, cold rolled, recrystallized at 1173 K for 4h	fcc	98±6% fcc	1500	99±3% fcc	1200

Table 1
Comparison of phase composition of the alloys in the Cr-Fe-Mn-Ni system observed in the literature with the results of our Monte Carlo simulations. For the samples that were heat-treated at different temperatures, phase composition at the two corresponding temperatures in MC simulations is shown. Since our MC simulations are performed on the grid with 5% concentration step, the data for compositions off-grid is interpolated with inverse distance weighting.

Composition	As-cast			Annealed		
	Expt.	MC @ 1100-1500 K	Error	Expt. @ 1273 K	MC @ 1300 K	Error
$[CrFeMn]_{80}Ni_{20}$	77.5% fcc	84%-89% fcc	18%-21%	75% fcc	85% fcc	21%
	21.8% bcc	11%-16% bcc		23.8% σ	15% bcc	
$[CrFeMn]_{75}Ni_{25}$	100% fcc	90%-94% fcc	9%-17%	87.5% fcc	92% fcc	13%
		6%-10% bcc		10.4% σ	8% bcc	
				1.53% bcc		
$[CrFeMn]_{65}Ni_{35}$	100% fcc	97%-99% fcc	2%-9%	99.6% fcc	98% fcc	5%
		1-3% bcc			2% bcc	

Table 2
Comparison of phase composition as a function of Ni concentration in the as-cast state. Since the temperature related to the as-cast state is unknown, the experimental data are compared with the MC results for the range of temperatures between 1100 K and 1500 K, inclusively, and the data is presented not for the endpoints, but for minimum and maximum values observed in this range.

in the $[CrFeMn]_{80}Ni_{20}$ alloy, however, the thermodynamic equilibrium is not the single fcc phase for most temperatures, see Fig. 6d. It may suggest that the as-cast sample of alloy characterized as a single fcc phase is probably not a thermodynamic equilibrium state. This is confirmed by the EBSD result for the sample of equiatomic alloy annealed at 1273 K for 48 h, for which the fcc fraction is 87.5% which is in line with the MC results showing the fcc fraction equal to 92 %. The fraction of fcc phase for the alloy with 35 at. % Ni is 100% for the as-cast and 99.6 % for the annealed sample, which is in agreement with the results from MC simulations.

The results of SEM combined with EDS show that the alloys with the coexistence of fcc, bcc and σ phases are

decomposed usually into the Ni-rich fcc regions and the Cr-rich regions of the bcc or σ phase. As shown in Figs. 9a–f, the Cr-rich regions are usually depleted of Ni and *vice versa*. Mn and Fe are distributed much more uniformly in the investigated alloys, however, their concentrations are, in general, more correlated with the presence of Ni, see Figs. 9g–l.

6. Prediction of new single fcc phases

As was shown in the previous sections, the DFT-based MC simulations enable an understanding of the influence of concentrations of constituent elements on the fcc-bcc phase
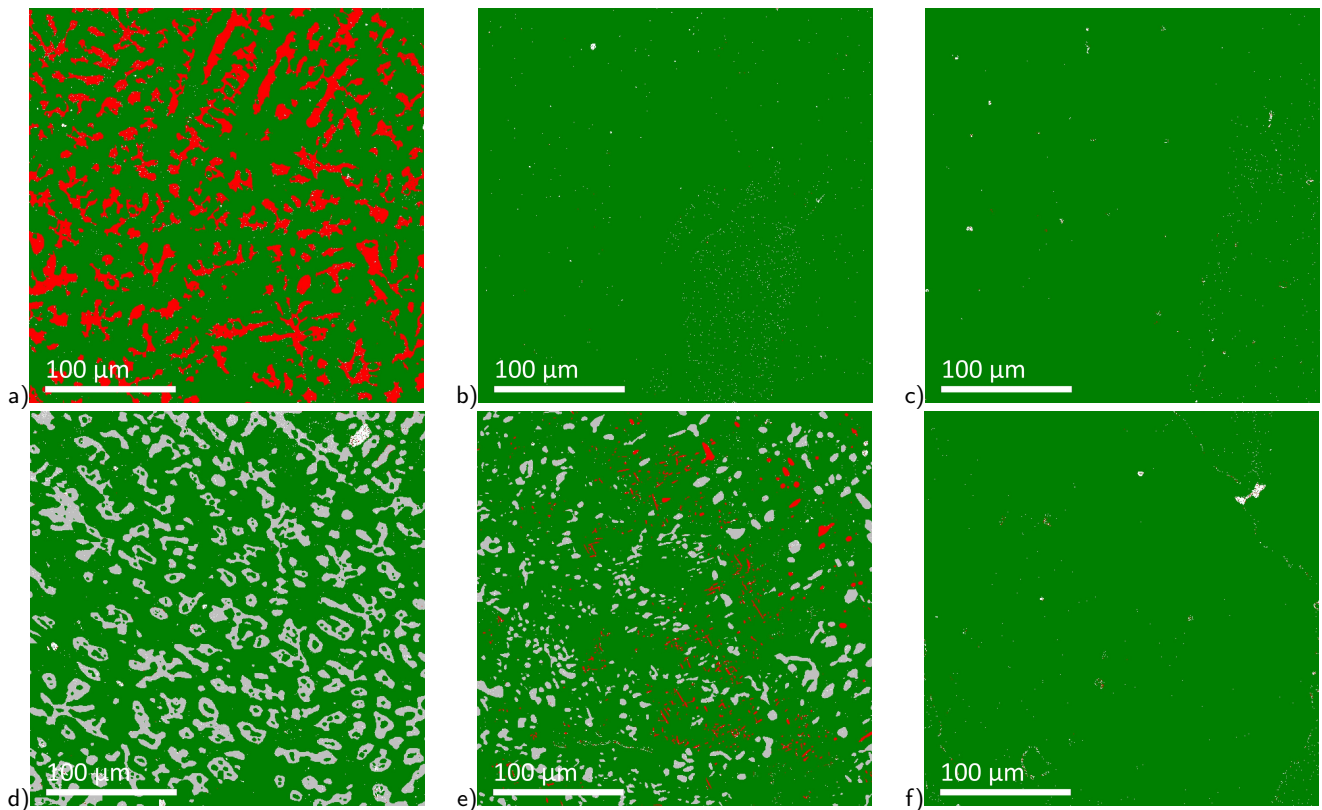
Figure 8: The results of EBSD characterization of the as-cast (a-c) and annealed (d-f) samples of alloys with 20 (a,d), 25 (b,e) and 35 (c,f) at. % Ni. Green, red and gray colors indicate the fcc, bcc and σ phases, respectively.

stability of Cr-Fe-Mn-Ni alloys. The fractions of the fcc phase are in good agreement with the available experimental data, which positively validates the accuracy of the model. Therefore, the MC simulations can be applied to design new near-equiatomic compositions of high-entropy alloys for which the stability of single fcc phase will be maintained for a relatively wide range of temperatures.

In Fig. 10, fcc fractions are shown as a temperature function for the alloy compositions, for which the fcc phase is fully stable at least at temperatures around 1000 K and the deviation from the equiatomic is smaller than 13 %. It is clearly visible that the fcc fractions for all chosen compositions are significantly smaller than the values for the equiatomic composition, indicated in Fig. 10 by a solid black line.

In line with the knowledge that Ni is the fcc stabilizer, there is only one composition with 20 at. % Ni, four and six with 25 and 30 at. % Ni, respectively. There are only two compositions with Ni concentration equal to 35 %, but it is related to the fact that only compositions with the deviation from the equiatomic alloy smaller than 13 % were considered. Among the alloys with Ni concentrations equal to 20 and 25 % that are stable fcc phases at temperatures around 1000 K, the concentration of Cr is always decreased in comparison with the equiatomic alloy – they contain either 15 or 20 at. % Cr, see Fig. 10a. The concentration of Cr is also usually decreased in the alloys with 30 and

35 at. % Ni, however there are two examples of alloys with Ni concentration equal to 25 %, see Fig. 10b. Following the results shown in Figs.6c and 7c, it is worth mentioning that in addition to the conventional role of Ni as the fcc stabilizer in Cr-Fe-Ni based austenitic steels, Mn also plays an important role in the fcc phase stability of concentrated Cr-Fe-Mn-Ni alloys.

According to MC simulations, none of the near-equiatomic alloy compositions shown in Fig. 10 is fully single fcc phase in the investigated temperature range. However, the temperature ranges of instability of fcc phase are usually narrow and the bcc fraction for those temperatures is small, usually below 6 %. At the same time, the errors shown in Fig. 7 for the near-equiatomic alloy compositions are usually larger than 6 %, which means that with 95 % confidence, the single fcc phase can be observed even for those temperatures where the average fcc fraction from MC simulations is decreased. Importantly, even if the decreased fcc fraction indicates a probability of formation of the bcc phase, the temperature range of the possible existence of bcc precipitates is narrow. For example, a small fraction of bcc phase is observed for $Cr_{20}Fe_{30}Mn_{20}Ni_{30}$ alloy only at 1300 K. For the $Cr_{15}Fe_{30}Mn_{30}Ni_{25}$, $Cr_{15}Fe_{30}Mn_{25}Ni_{30}$ and $Cr_{20}Fe_{25}Mn_{20}Ni_{35}$ alloys, the fcc phase is only unstable at 1300 K and 1400 K, whereas the fcc phase for the $Cr_{15}Fe_{25}Mn_{30}Ni_{30}$ alloy is only not stable at 1400 K and 1500 K. An another interesting near-equiatomic alloy
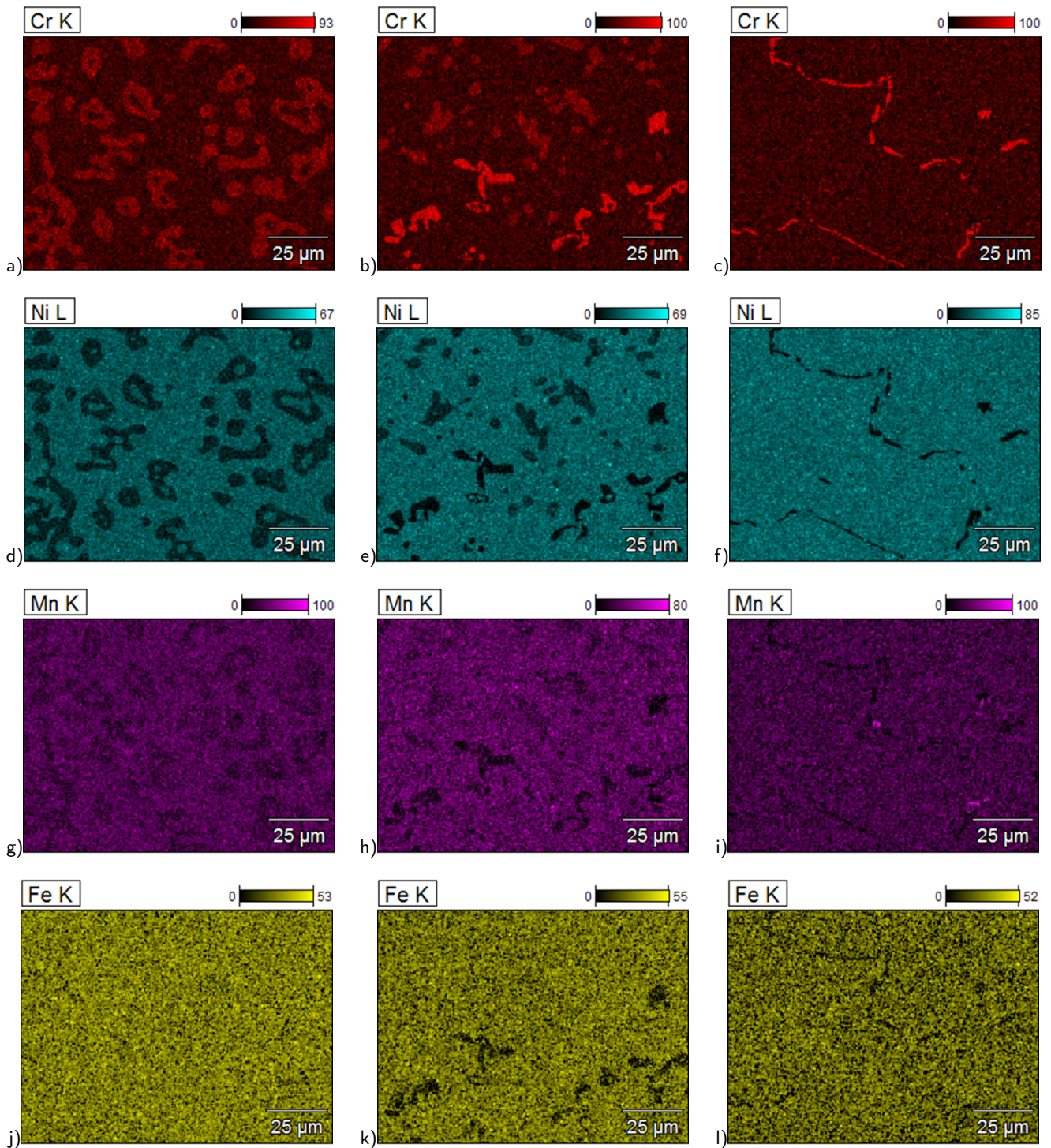
Figure 9: EDS mapping of Cr (a–c), Ni (d–f), Mn (g–i) and Fe (j–l) for the annealed samples of alloys with 20 (a,d,g,j), 25 (b,e,h,k) and 35 (c,f,i,l) at. % Ni.

composition is $Cr_{20}Fe_{35}Mn_{20}Ni_{25}$, for which there is no bcc fraction for any temperature above 600 K. It is worth to note that the results from MC simulations for the ORNL composition from Ref. [10] , $Cr_{18}Fe_{28}Mn_{26}Ni_{28}$, indicated in Figs. 10a and 10b by red solid line, confirm its relatively good stability of fcc phase. The fcc fraction is decreased in

the temperature range between 1200 K and 1500 K, however, the percentage of bcc phase is smaller than 4 %. As in the case of previously described alloys, it means that the ORNL alloy is the single fcc phase within the 95 % confidence interval for all the considered temperatures.

It should be noted that the increased fraction of the fcc phase for temperatures below 1000 K compared to higher temperatures can be caused by the underestimation of configurational entropy of bcc alloys calculated using the pair-wise approximation, as it was shown for the case of equiatomic composition in Section 4.1. As mentioned previously, the errors related to the estimation of relative stability in the mid-temperature region are hard to estimate. However, the results obtained in the low-temperature limit, where configurational entropies for both fcc and bcc alloys are equal to zero, and in the high-temperature limit, where the pair-wise approximation works well, are correct.

Finally, it is worth mentioning that in order to design a high-entropy alloy with good mechanical properties, one should look for fcc alloys, in which there will be a reduced possibility of formation of brittle intermetallic phases. Therefore, as it was discussed in Ref. [14], it is useful to search for the alloy compositions with the lowest order-disorder transition temperature, T_{ODT}^{fcc}. This parameter has been calculated as an inflection point on the $H_{form}(T)$ curve, and if few such points were found, the point at the highest temperature is considered T_{ODT}, as it is discussed in our previous work [14]. As it is given in the legend of Figs. 10a and 10b, the lowest T_{ODT}^{fcc} is observed for the $Cr_{20}Fe_{35}Mn_{25}Ni_{20}$ alloy, which unfortunately have also the largest 6 % decrease at 1200 K of fcc fraction among the considered alloys. The highest T_{ODT}^{fcc} are found for the compositions with 30 at. % of both Mn and Ni, namely $Cr_{15}Fe_{25}Mn_{30}Ni_{30}$ (T_{ODT}^{fcc} = 1400 K) and $Cr_{20}Fe_{20}Mn_{30}Ni_{30}$ (T_{ODT}^{fcc} = 1300 K), which is related to the formation of ordered intermetallic $L1_0$ MnNi phase, as discussed in our previous paper [14]. The other alloys possess T_{ODT}^{fcc} equal to 1100 K or 1200 K. Among them, it is worth to highlight two compositions, namely $Cr_{20}Fe_{35}Mn_{20}Ni_{25}$ and $Cr_{15}Fe_{30}Mn_{25}Ni_{30}$, with T_{ODT}^{fcc} = 1100 K and good stability of fcc phase, as described in the previous paragraph. The experimental investigation of the stability and properties of alloys with those compositions will be performed in future work.

7. Conclusions

- The differences between the free energies of formation of fcc and bcc alloys are the most negative for Ni-rich alloys and the most positive for Cr-rich alloys.

- The surface of intersection points reduces in the area and moves in the direction of Cr-rich compositions at temperature 1300 K compared to temperature 800 K, meaning that the stability of the fcc phase in the near-equiatomic region increases at higher temperatures.

- The coexistence of the fcc and bcc phases is predicted in a relatively wide range of compositions, and it may varies depending on temperature. Most notably, the coexistence of two phases is observed in the pseudo-binary $[FeMnNi]_{100-x}Cr_x$ alloys for concentrations between 30 and 50 at. % Cr whereas
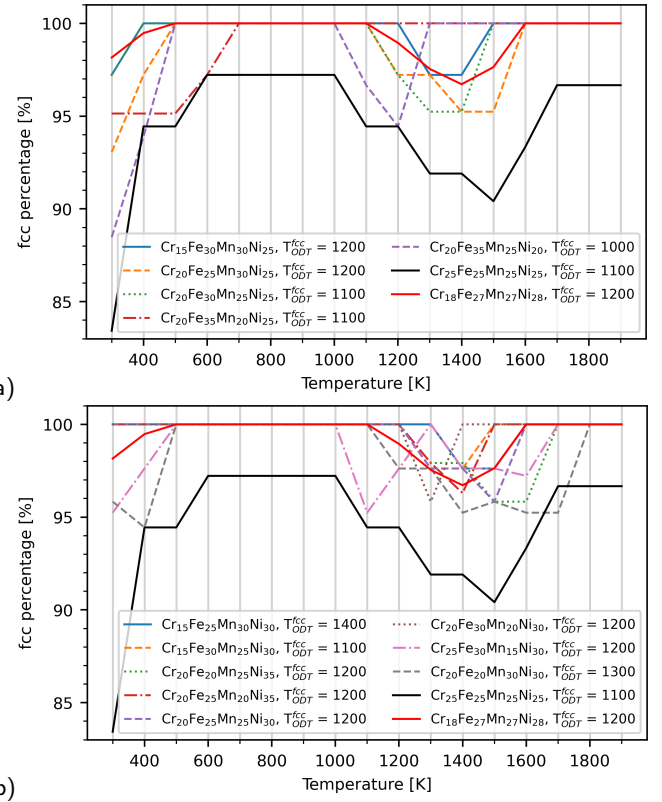

Figure 10: Percentage of fcc in the near-equiatomic Cr-Fe-Mn-Ni alloys with (a) 20 and 25 at. % Ni and (b) 30 and 35 at. % Ni. All presented compositions have deviations from 100% fcc that are smaller than the precision error of calculating the phase percentage. The equiatomic composition (black solid line) and the ORNL composition from Ref. [10], $Cr_{18}Fe_{27}Mn_{27}Ni_{28}$, (red solid line) are also plotted for reference. In the legend, there is also provided information about order-disorder transition temperature, T_{ODT}^{fcc}, for the considered fcc alloys (in K).

in the $[CrFeMn]_{100-x}Ni_x$ alloys for Ni concentration equal to or smaller than 25 at. %.

- With 95% confidence, the present study shows that the fcc phase is found to be dominant for the pseudo-binary alloy $[CrFeNi]_{1-x}Mn_x$ with all considered Mn concentrations and temperatures. This prediction which can be explained by the strong presence of $L1_0$ intermetallic phase in the fcc stability region of the quaternary Cr-Fe-Mn-Ni alloys, will certainly stimulate further investigation of Mn role in exploring the single fcc phase at high temperature.

- The fcc fractions predicted using DFT-based MC simulations are in agreement with the available experimental data and the experimental studies performed within this work for the samples of the $[CrFeMn]_{100-x}Ni_x$ alloys, where x = 20, 25 and 35 at. %, in the as-cast state and annealed at 1273 K.

- The EBSD results for the alloy with 35 at. % Ni confirmed predictions from MC simulations that the alloy is the single fcc phase.

- The fcc fractions calculated using MC simulations for the alloy with 20 at. % Ni are generally in line with the values measured using EBSD for the as-cast and annealed sample.

- The MC simulations for the equiatomic alloy showed that it is not a single fcc phase for most temperatures. It agrees with the EBSD characterization for the annealed sample but disagrees with the results for the as-cast sample, showing that it is a single phase. It may suggest that the as-cast sample is probably not in a thermodynamic equilibrium state.

- The bcc phase observed in the as-cast samples of alloys is transformed (or partially transformed) into the σ phase in the annealed samples. However, the fraction of the fcc phase is not significantly changed.

- The simulations enabled to propose the near-equiatomic alloy compositions that are single fcc phase for a wide range of temperatures with 95 % confidence.

- The $Cr_{20}Fe_{35}Mn_{20}Ni_{25}$ and $Cr_{15}Fe_{30}Mn_{25}Ni_{30}$ are highlighted as the near-equiatomic alloys with low order-disorder transition temperature and good stability of fcc phase, which might be potentially interesting for further research.

Acknowledgements

References

[1] B. Cantor, I.T.H. Chang, P. Knight, and A.J.B. Vincent. Microstructural development in equiatomic multicomponent alloys. *Mater. Sci. Eng. A*, 375-377:213–218, 2004.

[2] J.-W. Yeh, S.-K. Chen, S.-J. Lin, J.-Y. Gan, T.-S. Chin, T.-T. Shun, and C.-H. Tsau. Nanostructured High-Entropy Alloys with Multiple Principal Elements : Novel Alloy Design Concepts and Outcomes. *Adv. Eng. Mater.*, 6(5):299–303, 2004.

[3] E.K. Pickering and N.G. Jones. High-Entropy Alloys: A Critical Assessment of Their Founding Principles and Future Prospects. *Int. Mater. Rev.*, 61(3):183–202, 2016.

[4] D.B. Miracle and O.N. Senkov. A Critical Review of High Entropy Alloys and Related Concepts. *Acta Mater.*, 122:448–511, 2017.

[5] E.P. George, W.A. Curtin, and C.C. Tasan. High entropy alloys: A focused review of mechanical properties and deformation mechanisms. *Acta Mater.*, 188:435–474, 2020.

[6] Y. Shi, B. Yang, and P.K. Liaw. Corrosion-resistant high-entropy alloys: A review. *Metals*, 7(2):1–18, 2017.

[7] A.V. Kuznetsov, D.G. Shaysultanov, N.D. Stepanov, G.A. Salishchev, and O.N. Senkov. Tensile properties of an AlCrCuNiFeCo high-entropy alloy in as-cast and wrought conditions. *Mater. Sci. Eng. A*, 533:107–118, 2012.

[8] O.N. Senkov, S.V. Senkova, and C. Woodward. Effect of aluminum on the microstructure and properties of two refractory high-entropy alloys. *Acta Mater.*, 68:214–228, 2014.

[9] F.J. Wang, Y. Zhang, and G.L. Chen. Atomic packing efficiency and phase transition in a high entropy alloy. *J. Alloys Compd.*, 478(1-2):321–324, 2009.

[10] N.A.P. Kiran Kumar, C. Li, K.J. Leonard, H. Bei, and S.J. Zinkle. Microstructural stability and mechanical behavior of FeNiMnCr high entropy alloy under ion irradiation. *Acta Mater.*, 113:230–244, 2016.

[11] C. Lu, L. Niu, N. Chen, K. Jin, T. Yang, P. Xiu, Y. Zhang, F. Gao, H. Bei, S. Shi, M.-R. He, I.M. Robertson, W.J. Weber, and L. Wang. Enhancing radiation tolerance by controlling defect mobility and migration pathways in multicomponent single-phase alloys. *Nat. Commun.*, 7:13564, 2016.

[12] K. Jin, C. Lu, L.M. Wang, J. Qu, W.J. Weber, Y. Zhang, and H. Bei. Effects of compositional complexity on the ion-irradiation induced swelling and hardening in Ni-containing equiatomic alloys. *Scr. Mater.*, 119:65–70, 2016.

[13] O. El-Atwani, N. Li, M. Li, A. Devaraj, J.K.S. Baldwin, M.M. Schneider, D. Sobieraj, J.S. Wróbel, D. Nguyen-Manh, S.A. Maloy, and E. Martinez. Outstanding radiation resistance of tungsten-based high-entropy alloys. *Sci. Adv.*, 5(3):eaav2002, 2019.

[14] M. Fedorov, J.S. Wróbel, A. Fernández-Caballero, K.J. Kurzydłowski, and D. Nguyen-Manh. Phase stability and magnetic properties in fcc Fe-Cr-Mn-Ni alloys from first-principles modeling. *Phys. Rev. B*, 101:174416, 2020.

[15] D.H. Chung, W.C. Kim, S.Y. Baek, M.H. Kim, and Y.S. Na. Thermodynamics-based design strategy for optimizing strength and ductility of Cr-Ni-Mn-Fe medium-entropy alloys. *J. Alloys Compd.*, 899:163331, 2022.

[16] A. Fernández-Caballero, E. Bousser, S.M. Shubeita, P.T. Wady, Y. Gu, R. Krishna, M.J. Gorley, D. Nguyen-Manh, P.M. Mummery, and E.J. Pickering. High-dose ion irradiation damage in $Fe_{28}Ni_{28}Mn_{26}Cr_{18}$ characterised by TEM and depth-sensing nanoindentation. *Nucl. Mater. Energy*, 28:101028, 2021.

[17] A. Kamboj and E.A. Marquis. Effect of dose rate on the phase stability of a CrFeNiMn alloy. *Scr. Mater.*, 215:114697, 2022.

[18] J. Lehtonen, Y. Ge, N. Ciftci, O. Heczko, V. Uhlenwinkel, and S.-P. Hannula. Phase structures of gas atomized equiatomic CrFeNiMn high entropy alloy powder. *J. Alloys Compd.*, 827:154142, 2020.

[19] J. Lehtonen, P. Lehto, Y. Ge, A. Juselius, and S.-P. Hannula. Mechanical properties of pulsed electric current sintered CrFeNiMn equiatomic alloy. *Mater. Sci. Eng. A*, 842:143071, 2022.

[20] C. Li, X. Hu, T. Yang, N.A.P. Kiran Kumar, B.D. Wirth, and S.J. Zinkle. Neutron irradiation response of a Co-free high entropy alloy. *J. Nucl. Mater.*, 527:151838, 2019.

---

[21] T.J. Manescau, J. Braun, and O. Dezellus. Computational development, synthesis and mechanical properties of face centered cubic Co-free high entropy alloys. *Mater. Today Commun.*, 30:103202, 2022.

[22] R.K. Nutor, M. Azeemullah, Q.P. Cao, X.D. Wang, D.X. Zhang, and J.Z. Jiang. Microstructure and properties of a Co-free $Fe_{50}Mn_{27}Ni_{10}Cr_{13}$ high entropy alloy. *J. Alloys Compd.*, 851:156842, 2021.

[23] N.D. Stepanov, D.G. Shaysultanov, M.A. Tikhonovsky, and G.A. Salishchev. Tensile properties of the Cr-Fe-Ni-Mn non-equiatomic multicomponent alloys with different Cr contents. *Mater. Des.*, 87:60–65, 2015.

[24] Z. Wu, H. Bei, F. Otto, G.M. Pharr, and E.P. George. Recovery, recrystallization, grain growth and phase stability of a family of FCC-structured multi-component equiatomic solid solution alloys. *Intermetallics*, 46:131–140, 2014.

[25] Z. Wu and H. Bei. Microstructures and mechanical properties of compositionally complex Co-free $FeNiMnCr_{18}$ FCC solid solution alloy. *Mater. Sci. Eng. A*, 640:217–224, 2015.

[26] Y. Zhang, H. Wu, X. Yu, D. Tang, R. Yuan, and H. Sun. Microstructural evolution and strengthening mechanisms in $Cr_x MnFeNi$ high-entropy alloy. *J. Mater. Res. Technol.*, 12:2114–2127, 2021.

[27] J. Zhou, H. Liao, H. Chen, and A. Huang. Microstructure and Tensile Mechanical Behavior of a Single-Phase $Fe_{35}Mn_{10}Cr_{20}Ni_{35}$ High-Entropy Alloy. *J. Mater. Eng. Perform.*, 30(5):3352–3362, 2021.

[28] A. Daramola, G. Bonny, G. Adjanor, C. Domain, G. Monnet, and A. Fraczkiewicz. Development of a plasticity-oriented interatomic potential for CrFeMnNi high entropy alloys. *Comput. Mater. Sci.*, 203:111165, 2022.

[29] J.S. Wróbel, D. Nguyen-Manh, M.Y. Lavrentiev, M. Muzyk, and S.L. Dudarev. Phase stability of ternary fcc and bcc Fe-Cr-Ni alloys. *Phys. Rev. B*, 91:024108, 2015.

[30] D. Sobieraj, J.S. Wróbel, T. Rygier, K.J. Kurzydłowski, O. El-Atwani, A. Devaraj, E. Martinez Saez, and D. Nguyen-Manh. Chemical short-range order in derivative Cr–Ta–Ti–V–W high entropy alloys from the first-principles thermodynamic study. *Phys. Chem. Chem. Phys.*, 22:23929–23951, 2020.

[31] D. Nguyen-Manh, J.S. Wróbel, M. Klimenkov, M.J. Lloyd, L. Messina, and S.L. Dudarev. First-principles model for voids decorated by transmutation solutes: Short-range order effects and application to neutron irradiated tungsten. *Phys. Rev. Materials*, 5:065401, 2021.

[32] A. van de Walle. Multicomponent multisublattice alloys, nonconfigurational entropy and other additions to the Alloy Theoretic Automated Toolkit. *CALPHAD*, 33(2):266–278, 2009.

[33] A. Fernández-Caballero, M. Fedorov, J.S. Wróbel, P.M. Mummery, and D. Nguyen-Manh. Configurational Entropy in Multicomponent Alloys: Matrix Formulation from Ab Initio Based Hamiltonian and Application to the FCC Cr-Fe-Mn-Ni System. *Entropy*, 21(1):68, 2019.

[34] H.A. Bethe and W.L. Bragg. Statistical theory of superlattices. *Proc. R. Soc. Lond. A*, 150(871):552–575, 1935.

[35] E.A. Guggenheim and R.H. Fowler. Statistical thermodynamics of mixtures with zero energies of mixing. *Proc. R. Soc. Lond. A*, 183(993):203–212, 1944.

[36] W.L. Bragg and E.J. Williams. The effect of thermal agitation on atomic arrangement in alloys. *Proc. R. Soc. Lond. A*, 145(855):699–730, 1934.

[37] M.Yu. Lavrentiev, D. Nguyen-Manh, and S.L. Dudarev. Magnetic cluster expansion model for bcc-fcc transitions in fe and fe-cr alloys. *Phys. Rev. B*, 81:184202, 2010.

[38] I. Toda-Caraballo, J.S. Wróbel, S.L. Dudarev, D. Nguyen-Manh, and P.E.J. Rivera-Díaz-del Castillo. Interatomic spacing distribution in multicomponent alloys. *Acta Mater.*, 97:156–169, 2015.

[39] G. Kresse and J. Hafner. Ab initio molecular dynamics for liquid metals. *Phys. Rev. B*, 47(1):558–561, 1993.

[40] G. Kresse and J. Hafner. *Ab initio* molecular-dynamics simulation of the liquid-metal–amorphous-semiconductor transition in germanium. *Phys. Rev. B*, 49(20):14251–14269, 1994.

[41] G. Kresse and J. Furthmüller. Efficiency of ab-initio total energy calculations for metals and semiconductors using a plane-wave basis set. *Comput. Mater. Sci.*, 6(1):15–50, 1996.

[42] G. Kresse and J. Furthmüller. Efficient iterative schemes for ab initio total-energy calculations using a plane-wave basis set. *Phys. Rev. B*, 54(16):11169–11186, 1996.

[43] P.E. Blöchl. Projector augmented-wave method. *Phys. Rev. B*, 50(24):17953–17979, 1994.

[44] G. Kresse and D. Joubert. From ultrasoft pseudopotentials to the projector augmented-wave method. *Phys. Rev. B*, 59(3):1758–1775, 1999.

[45] J.P. Perdew, K. Burke, and M. Ernzerhof. Generalized gradient approximation made simple. *Phys. Rev. Lett.*, 77(18):3865–3868, 1996.

[46] J.D. Pack and H.J. Monkhorst. Special points for Brillouin-zone integrations. *Phys. Rev. B*, 13(12):5188–5192, 1976.

[47] A. van de Walle and G. Ceder. Automating first-principles phase diagram calculations. *J. Phase Equilib.*, 23(4):348–359, 2002.

[48] A. van de Walle and M. Asta. Self-driven lattice-model Monte Carlo simulations of alloy thermodynamic properties and phase diagrams. *Model. Simul. Mater. Sci. Eng. A*, 10(5):521–538, 2002.

[49] G.L.W. Hart and R.W. Forcade. Algorithm for generating derivative structures. *Phys. Rev. B*, 77(22):224115, 2008.

[50] D. Nguyen-Manh, M.Yu. Lavrentiev, and S. L. Dudarev. Magnetic origin of nano-clustering and point defect interaction in Fe–Cr alloys: an ab-initio study. *J. Comput. Aided Mater. Des.*, 14:159–169, 2008.

[51] P. Erhart, B. Sadigh, and A. Caro. Are there stable long-range ordered $Fe_{1-x}Cr_x$ compounds? *Appl. Phys. Lett.*, 92(14):141904, 2008.

[52] L. Zhang, Y. Du, H. Xu, S. Liu, Y. Liu, F. Zheng, N. Dupin, H. Zhou, and C. Tang. Phase equilibria and thermal analysis in the fe–mn–ni system. *Int. J. Mater. Res.*, 100(2):160–175, 2009.

[53] A. Fernández-Caballero, M. Fedorov, J.S. Wróbel, P.M. Mummery, and D. Nguyen-Manh. Configurational entropy in multicomponent alloys: Matrix formulation from ab initio based hamiltonian and application to the FCC Cr-Fe-Mn-Ni system. *Entropy*, 21(1), 2019.

[54] M Ferry. *Direct Strip Casting of Metals and Alloys*. Woodhead Publishing Limited, Cambridge, 2006.

[55] L.I. Shvedov and Z.D. Pavlenko. Sigma-phase in the Fe-Cr-Mn-alloys. In *Vestsi Akadehmii Navuk BSSR. Seryya Fizika-Tehkhnichnykh Navuk*, pages 14–17. 1975.

[56] Y. Murata, K. Koyama, Y. Matsumoto, M. Morinaga, and N. Yukaww. Equilibrium Phase Diagram of Fe-Cr-MnTernary System. *ISIJ Int.*, 80:927–936, 1990.

[57] E.K. Pickering, R. Muñoz-Moreno, H.J. Stone, and N.G. Jones. Precipitation in the equiatomic high-entropy alloy CrMnFeCoNi. *Scr. Mater.*, 113:106–109, 2016.

[58] K.A. Christofidou, T.P. McAuliffe, P.M. Mignanelli, H.J. Stone, and N.G. Jones. On the prediction and the formation of the sigma phase in CrMnCoFeNix high entropy alloys. *J. Alloys Compd.*, 770:285–293, 2019.

[59] H. Li, J. Ruan, N. Ueshima, and K. Oikawa. Investigation on the sigma phase related equilibrium in Cr-Mn-Co system. *J. Alloys Compd.*, 867:159024, 2021.

[60] D.P. Shoemaker and B.G. Bergman. The crystal structure of a sigma phase, FeCr. *J. Am. Chem. Soc.*, 72:5793, 1950.

[61] N.Y. Samoylova, I.A. Bobrikov, E.A. Korneeava, R.N. Vasin, A.M. Balagurov, and I.S Golovin. Kinetic of the isothermal A2 to sigma phase transformation in Fe-Cr alloy. *J. Alloys Compd.*, 913:165282, 2022.